Plasmonic color metasurfaces fabricated by a high speed roll-to-roll method

Murthy, Swathi; Pranov, Henrik; Feidenhans'l, Nikolaj Agentoft; Madsen, Jonas S.; Hansen, Poul Erik; Pedersen, Henrik Chresten; Taboryski, Rafael J.

Published in:
Nanoscale

Link to article, DOI:
10.1039/c7nr05498j

Publication date:
2017

Document Version
Peer reviewed version

Plasmonic color metasurfaces fabricated by a high speed roll-to-roll method

Swathi Murthy[1], Henrik Pranov[2], Nikolaj A. Feidenhans'l[3,4], Jonas S. Madsen[3], Poul Erik Hansen[3], Henrik C. Pedersen[1], and Rafael Taboryski[4,*]

[1] Department of Photonics Engineering, Technical University of Denmark, Frederiksborgvej 399, DK-4000 Roskilde, Denmark

[2] Heliac ApS, Ambolten 8, DK-2970 Hørsholm, Denmark

[3] Danish Fundamental Metrology A/S, Matematiktorvet 307, DK-2800 Kgs. Lyngby, Denmark

[4] Department of Micro- and Nanotechnology, Technical University of Denmark, DK-2800 Kgs. Lyngby, Denmark

[*]rata@nanotech.dtu.dk

Abstract

Lab-scale plasmonic color printing using nano-structured and subsequently metallized surfaces have been demonstrated to provide vivid colors. However, upscaling these structures for large area manufacturing is extremely challenging due to the requirement of nanometer precision of metal thickness. In this study, we have investigated a plasmonic color meta-surface design that can be easily upscaled. We have demonstrated the feasibility of fabrication of these plasmonic color surfaces by a high-speed roll-to-roll method, comprising roll-to-roll extrusion coating at 10 m/min creating a polymer foil having 100 nm deep pits of varying sub-wavelength diameter and pitch length. Subsequently this polymer film was metallized and coated also by high-speed roll-to-roll methods. The perceived colors have high tolerance towards the thickness of the metal layer, when this thickness exceeds the depths of the pits, which enables the robust high-speed fabrication. This finding can pave the way for plasmonic meta-surfaces to be implemented in a broader range of applications such as printing, memory, surface enhanced Raman scattering (SERS), biosensors, flexible displays, photovoltaics, security, and product branding.

Keywords: nanomaterials, polymers, metamaterials, nanotechnology, extrusion coating, photonics, plasmonic colors, sub-wavelength optics.

Introduction

The interaction of light with matter whereby the electric field of incoming light excites coherent conduction-electron-density oscillations in metals can be ascribed to a quasiparticle called the surface plasmon polariton (SPP).[1, 2] Owing to the dissipative nature of these oscillations, light can only propagate into a thin skin layer at the metal surface making metals non-transparent for electromagnetic waves with angular frequency below the characteristic plasma frequency $\omega_p = \sqrt{n_e e^2/m^*\varepsilon_0}$, where n_e is the electron density of the metal, e the elementary charge, m^* the effective mass of electrons, and ε_0 the permittivity of free space. Evanescent modes propagating along the surface are however supported by SPPs. For metallic nanoparticles and for metallic surface structures with size below the diffraction limit of visible light (~200 nm), the evanescent plasma oscillation modes along the surface are replaced by localized multipole oscillations[3] with pronounced resonant properties depending on shape, size and material composition of structures[4-6], and resulting in absorption of light at characteristic wavelengths and photoluminescence due to re-emission at Stokes shifted wavelengths for hot electrons[7]. The absorption of light at specific wavelengths gives rise to the subtractive color effects in the reflected spectrum from plasmonic materials.[8] Color effects based on these localized surface plasmon resonances (LSPR) in metallic nanoparticles have been used for hundreds of years such as for staining of glass and ornamental cups (Lycurgus cup).[9, 10] More recently, plasmonic colors have been demonstrated for surfaces structured at nanoscale by lithographic techniques,[11, 12] allowing for color printing using metal nano-structures as a high resolution replacement for inking with color dyes, and with potential for use in digital imaging and display technologies.[13] Moreover, metallic nanostructured surfaces may also be exploited as an efficient media for surface-enhanced Raman scattering (SERS),[14, 15] for biosensing,[16, 17] , data storage[18] and for meta-surface materials that can be modified by pulsed laser printing[6]. Although some industrial applications, such as optical security devices using plasmon resonances in sinusoidal gratings in thin metallic films[19, 20] have been reported, exploitation of plasmonic color printing technology in the above mentioned areas and in addition for security and product-branding applications is however largely impeded by practical issues of cost and utility.[5] One measure to reduce costs is by using aluminum (Al) as the plasmonic material instead of noble metals.[5, 21, 22] Some groups have reported plasmonic color effects from structured continuous metal films[23-25], however, most studies on plasmonic color

effects have been conducted on discontinuous metal nanostructures, where the metal nano-disks have been separated from the underlying perforated metal film (back-reflector) by dielectric pillars using vacuum based physical vapor deposition (PVD) techniques, that allow for a directional deposition of metal onto nano-posts.[5, 11, 12] The directional PVD processes form metal disks of well-defined thickness (~20 nm) that are separated from the metal back-reflector (BR) due to uncoated side walls. This architecture, however, represents a barrier for utilization, as the required directional metal coating with nanometer precision is not conducive for industrial high throughput production, and clean-room based PVD processes, on the other hand, are very expensive.

In this study, we report a plasmonic metasurface design using Al nanostructures which can easily be up-scaled to overcome the limitation for mass production of plasmonic color surfaces. This is achieved by making plasmonic color printing robust for high volume production by rendering the perceived plasmonic colors more tolerant to metal thickness when the thickness exceeds the depth of the nanostructures, and towards small dimensional variations (in particular diameter), which are expected during high throughput production. In support for our claim, we demonstrate fabrication of these hybrid plasmonic mode metasurfaces by a high throughput roll-to-roll process chain. The resulting metallized foil is shown in **Figure 1a-c.**

For nano-structuring of the surfaces, we employ a roll-to-roll extrusion coating process (R2R-EC), explained in the methods sectionIn recent publications we have demonstrated this process for replication of nano-pillars and protruding microstructures[26], nanograss[27], and nanopits[28]. These works, however, did not address metallization and plasmonic color effects. Several other techniques for roll-to-roll (R2R) nano-structuring have been demonstrated. R2R thermal nanoimprinting is capable of imprinting most thermoplastic materials, but is limited in speed and requires very precise temperature control as the glass transition temperature cannot be exceeded due to the web tension, which may cause breaking of the web.[29] Another technique is R2R UV-assisted nanoimprint lithography[30] with reported state of the art roller speed in excess of 10 m/min on a 25 cm wide web[31]. However, the UV assisted methods are limited due to the requirements of using UV curable resins for structuring, which may be prohibitively expensive, in some areas, for commercial utilization.

Results and discussion

The main results of this study are presented in **Figure 1.** In **Figure 1a**, the 45 cm wide metalized and encapsulated foil is rolled out. The insert shows a magnified DTU logo printed on the foil by varying pit diameter and pitch length, as explained below. **Figure 1b**, shows a magnified color image of the colored patches, while **Figure 1c** shows a scanning electron micrograph (SEM) of the metalized nano-pits. The nanostructured polypropylene (PP) layer with pits[28] of varying diameter (D) and pitch (P) (**Figure 1d**), but constant depth of ~100 nm, is manufactured by R2R-EC at a rate of 10 m/min, with a 45 cm wide web (**Figure 1e** and **Figure S1**). After metallization of the structured foil, with 100 nm of Al (**Figure 1c**) the foil exhibits vivid colors when viewed through the transparent carrier foil (from the backside) (**Figure 1f**). The reflected color depends on nano-pit diameter D and pitch length P, which were varied between (D, P) = (60, 80) nm to (160, 220) nm (**Figure 1d, f**), while no variation in pit depth was required, and was thus held constant at ~100 nm.

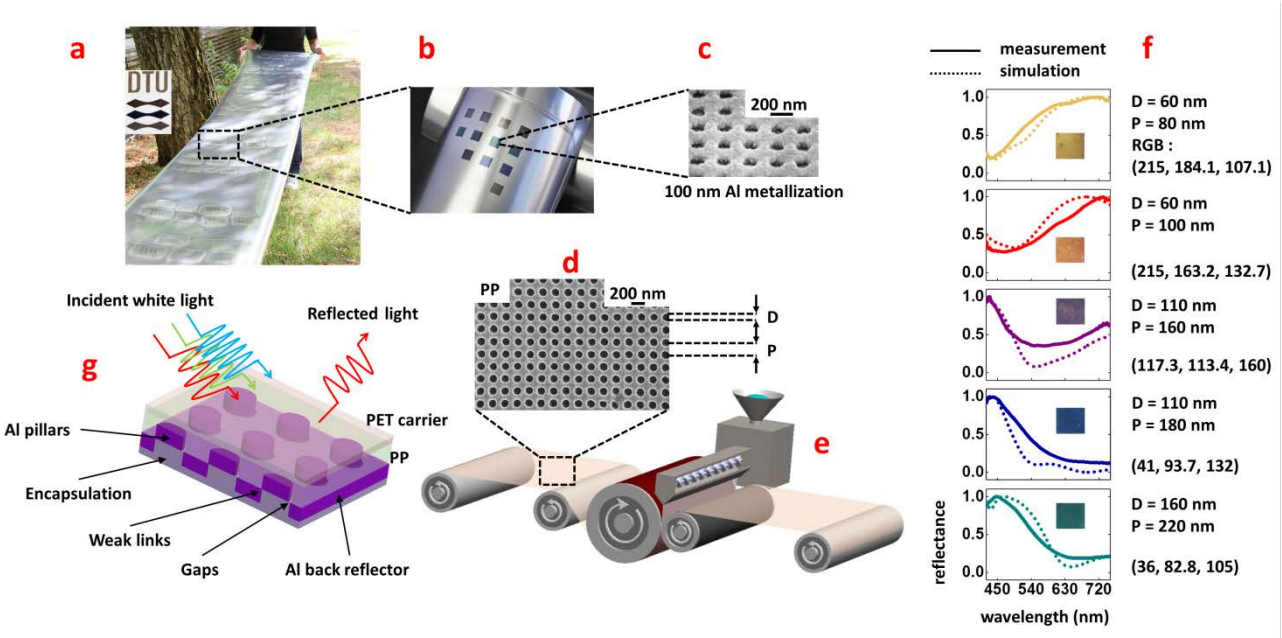

Figure 1. a: Polymer foil structured by nano-R2R-EC and subsequently R2R metallized with 100 nm Al. Insert shows a DTU logo (1 cm by 1.5 cm) fabricated by plasmonic color printing. **b:** Zoom in on one of the structured patches exhibiting vivid plasmonic colors. The colored patches are 0.5 cm x 0.5 cm. **c:** SEM image of foil after metallization with 100 nm of Al. **d:** SEM image of the nano-pit

array with diameter D and pitch length P formed in PP by R2R-EC. **e:** Schematic of the R2R-EC process. **f:** Various combinations of diameter D and pitch length P give rise to different measured reflectance spectra (solid lines), which are compared to the simulated spectra (dashed lines), based on the geometry. Inserts show photographs of the corresponding samples. Nano-pit diameter D and pitch length P are also given for each of the spectra alongside with the RGB color coordinates for the corresponding measured spectra **g:** Schematic representation of the layer design. Nano-pits are formed in transparent polypropylene (PP) on a transparent polyethylene terephthalate (PET) carrier foil. The Al coating is continuous and fill the pits in PP thereby forming Al nanopillars with weak links and gaps of varying size in the range of a few nanometers between the Al back reflector and the Al pillars. The colors are visible through the transparent carrier foil.

Both batch metallization, at a rate of 10 Å/s (0.1 ng/s), performed in a clean room environment and R2R metallization at a speed of 350 m/min (1 g/s) were investigated. Interestingly, both batch and R2R metallization gave similar colors for the corresponding D and P, though the deposition rate for the industrial set-up was 10 orders of magnitude higher than that of the clean-room deposition. The metallized foil was subsequently encapsulated using a thin layer of UV glue/lacquer, to protect the Al film. The encapsulation did not significantly change the perceived colors and the reflectance spectrum (as shown in **Figure S2**). After metallization with 100 nm of Al (**Figure 1c**) the pits in PP are converted into pillars in Al. The measured and simulated reflectance data for different D and P are plotted in **Figure 1f** for the 100 nm Al samples. The simulated and measured data are seen to match well. The overall foil architecture is sketched and explained in **Figure 1g**. Details of the foil architecture are shown in **Figure 2a.**

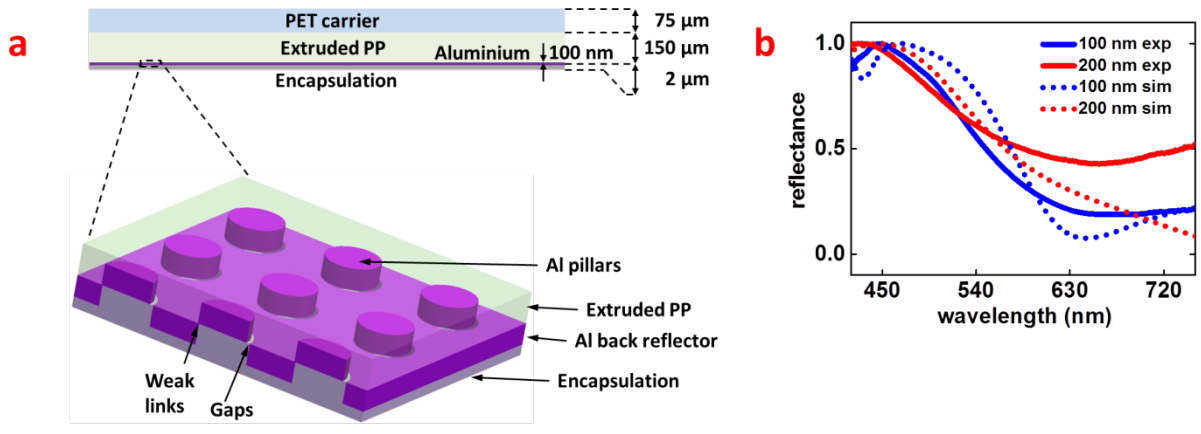

Figure 2. a: The foil architecture and a schematic representation of cross-sectional view of the metalized and encapsulated foil sandwich, showing the actual thickness of different layers; a zoom-in - 3D representation of the nano-structured PP foil, showing the configuration with links and gaps between the Al nano-pillars and Al back reflector. **b:** Comparison of measured and simulated spectra samples metalized with 100 nm Al and with 200 nm Al.

The perceived colors are independent of the viewing angle, since the pitch of the structures is below the diffraction limit of light (<220 nm).[11, 12] We observe a wide range of colors in the 100 nm Al samples, right from red to blue by altering D and P. Hence, we can practically achieve all colors in the visible range by fine tuning the structure dimensions or by mixing different structure sizes in one pixel. Another interesting feature is that the samples exhibit the same colors (indistinguishable to the naked eye) even when coated with 200 nm of Al. In **Figure 2b** we thus show that the spectra for 100 nm and 200 nm metallization indeed are very similar. This indicates that the colors are tolerant towards metal thickness variation making them robust for mass production.

The computer simulated spectra which are shown and compared with measured spectra in **Figure 1f**, are made by numerically solving Maxwell's equations for incident and reflected plane waves normal to the surface without taking any quantum mechanical tunneling effects[32] across the gaps into account. The simulations employ a simplified 3D model of the structure as shown in **Figure 3a, b.** We tested three hypotheses regarding the Al layer configuration: 1) continuous Al film with perfect sidewall coverage (**Figure 3a, b** left), 2) no metallic connection between pillar and back reflector (BR) (**Figure 3a, b** middle), and 3) partial sidewall coverage resulting in a weak link between pillar and BR, and a corresponding varying gap opposing the weak link (**Figure 3a, b** right). **Figure 3c** show the distribution of the electric field strength for the three configurations. We see that while the continuous metal configuration exhibits a rather smooth electric field distribution, the two discontinuous configurations show a clear formation of hot spots, where the electric field strength is highly enhanced in the sub 10 nm spacing between the pillars and the back reflector. Most notably this is seen for the varying gap configuration, where we see a highly localized and very pronounced hot spot near the position of the weak link, where the gap is very narrow (<2nm), (**Figure 3d**). The simulation indicates a seven orders of magnitude enhancement of the electric field strength in the hot spot area when compared to the larger continuous surface

areas of the Al (**Figure 3e**). Further, we simulated the reflected spectra as a function of wavelength, and compared the simulated spectra for the three configurations to the measured spectra, for a given D and P. An example of this comparison is shown in **Figure 3f**. We see that the varying gap configuration convincingly fits the measured spectra, while the other configurations give rise to reflectance spectra exhibiting dips in wrong positions. Simulated spectra for different constant gap sizes (2 nm and 5 nm) were compared with the corresponding measured spectrum (**Figure S3**). From the figure we can see that, though the 2 nm constant gap spectrum fits better with the measured spectrum than 5 nm constant gap model, the varying gap configuration still fits the best. In reality, one cannot expect either a completely connected or completely disconnected (with constant nm sized gap) metal configuration between the Al pillar and the BR. It is by far more realistic to have connections in some regions, narrow gaps in some other regions and larger gaps in yet other regions. This leads us to conclude that the varying gap configuration is the one that best represents the physical samples. In **Figure 3g** we show a focused ion beam assisted scanning electron micrograph (FIB-SEM) validation of this Al layer configuration, where both the weak links and the gaps are clearly visible. The FIB-SEM, images are considered only as visual qualitative validation for the model as real values cannot be extracted due to the limited resolution. All the simulations shown in this article are carried out on nano-structures with sharp edges. However, a comparison was made between the simulation results for structures with sharp and rounded edges (**Figure S4**). Since there was no significant difference between the two, for simplicity, sharp edges were maintained throughout the article.

The simulations in **Figure 3c, d** further indicate that the presence of the hot spots at the positions of the weak links highly perturb the overall field distribution. These hot spots are created due to coupling between the plasmon resonances of the Al pillar and the cavity in the BR. It is a well-known phenomenon that sub 10 nm gaps between metallic nanostructures can lead to strong field enhancement.[14, 33-35] . In our case, the observed plasmon resonance is due to coupling of pillar and cavity plasmons. As shown in **Figure S5**, the simulations indicate that a strong coupling between the pillar and the cavity is achieved, when the nano-pit depth is similar to the thickness of the Al layer (100 nm). The pillar and cavity resonances split into two modes namely high energy anti-bonding and low energy bonding modes.[12, 36] As the depths of the nano-pits increase, the coupling

strength reduces. At higher nano-pit depths, the pillar and the cavity plasmons interact separately with the incident light causing respective absorption dips. During evaporation of the Al film, with increasing film thickness, the Al back reflector not only grows in the vertical direction but also grows slightly in the lateral direction due to the well-known nucleation process during evaporation.[37] This can be seen clearly for the 200 nm Al sample in the cross-sectional FIB-SEM image in **Figure 4d**. This rounded and expanded edge of the Al back reflector casts a shadow for Al deposition in the polymer nano-pits. The evaporation process, unlike other metal deposition processes like sputtering, is directional owing to a low chamber pressure (≤ 10^{-8} bar) and ballistic nature of the process, resulting in a collimated beam of the evaporating Al.[38] Hence the shadowed regions of the nano-pits in PP do not get completely filled, causing links and varying spacing between the Al pillars and Al BR. This assists in having a strong coupling between the pillars and the BR. The simulations shown in **Figure S5**, **S6** indicate that the strongly coupled structures (small/no vertical separation between Al pillar and BR) exhibit sharper colors, characterized by a distinct peak in the reflectance spectra, than weakly coupled structures (when the vertical separation between pillar and BR increases). For weakly coupled structures, the resonance curve broadens along the visible spectrum. Also, the strongly coupled structures are more robust towards variations in diameter of the pillars (**Figure S6**), which is desirable for mass production.

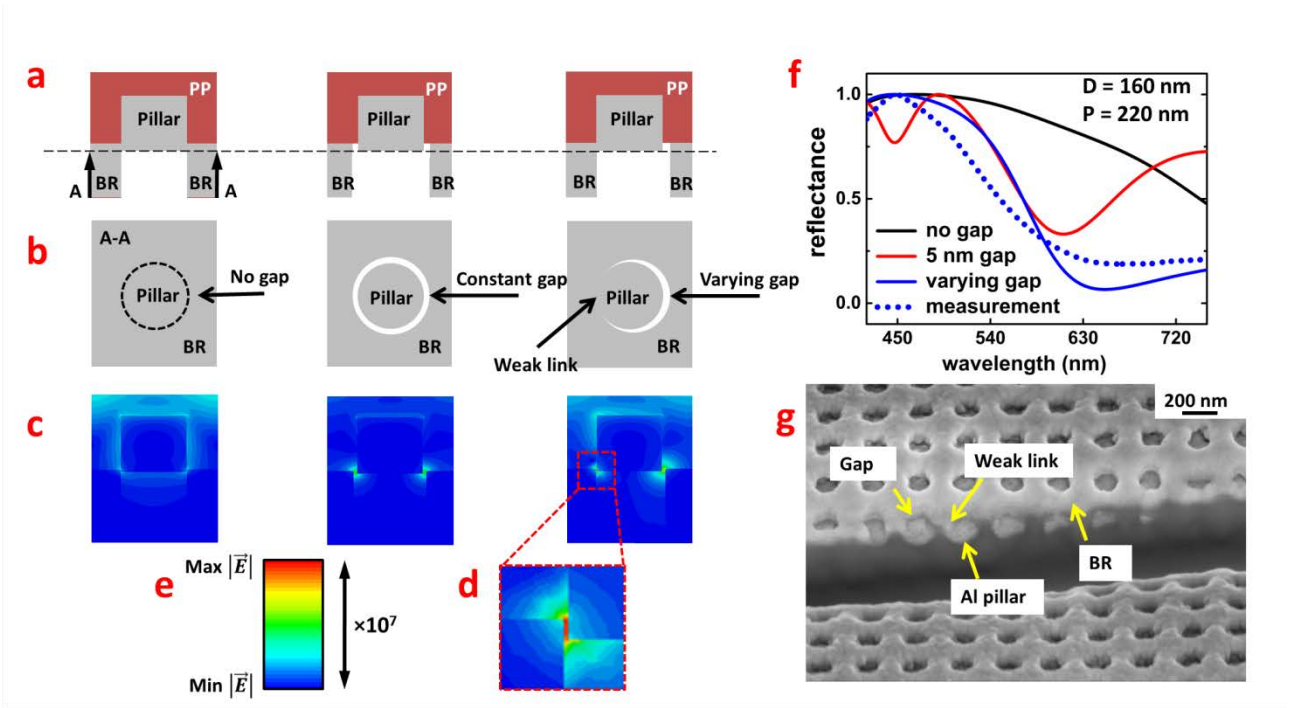

Figure 3. a: Three possible configurations of the Al layer in cross sectional view: continuous Al film with perfect sidewall coverage (left), no metallic connection between pillar and BR (middle), and partial sidewall coverage resulting in a weak link between pillar and BR, and a corresponding varying gap (right). **b:** The three possible configurations in bottom view. **c:** Simulated distribution of the electric field strength (logarithmic scale false colors, arbitrary units) for the three configurations at 600 THz light frequency (corresponding to 500 nm light wavelength in the middle of the visible range). **d:** Zoom in on the hot spot region, where the gap approaches zero. **e:** Logarithmic arbitrary units false color scale, showing the span of seven orders of magnitude variation between the hot spot region, and the bulk of the Al. **f:** Simulated spectra corresponding to the three Al layer configurations together with measured spectrum. **g:** FIB-SEM validation of the Al layer configuration.

For batch metallized samples, different colors were obtained, not only by varying D and P, but also varying metal thickness below 100 nm. The pits in PP have a fixed depth of ~100 nm, whereas D and P are varied from (60, 80) nm to (160, 220) nm. This spectral variation with metal thickness is caused by: the change in plasmon resonances of Al pillars and the cavity, which is geometry dependent;[10] and also the vertical separation between them. This effect is shown in **Figure 4**. In **Figure 4a** we show the measured reflectance spectra for samples, where the metal thickness was varied from 100 nm, through 50 nm to 20 nm. We see a clear change of the spectra, most notably between the 100 nm and the 20 nm data. Simulations have been carried out for 20 nm Al samples and compared to the corresponding measured spectra, shown in **Figure S7**. For the 20 nm Al samples, there could be coverage of the side walls of the pits with Al (up to a certain depth) during evaporation, as shown in **Figure 4b**. We included this in the model by reducing the distance between the Al pillars and the BR to 40 nm, instead of 80 nm in an ideal scenario. The scratches seen in the photographs of the colors, are due to manual handling of the samples during batch metallization, and are most pronounced for the 20 nm samples as expected. These defects are caused by some mechanical abrasion of the delicate nanostructures and can be avoided using the complete R2R production platform as shown in **Figure 1b**.

Many samples (20) having similar nano-pit geometry, made during the same and four different R2R-EC runs, were individually batch metallized with 100 nm Al. Each time the same colors were obtained for the corresponding D and P. This is a strong indication that this kind of links and varying gap geometry is more likely to be achieved during the evaporation process than completely connected or disconnected geometries. This is also what one can expect from an

evaporation process as the evaporating beam of Al, although being directional, cannot be completely controlled on the scale of a few nm, even at pressures as low as 10^{-8} bars.

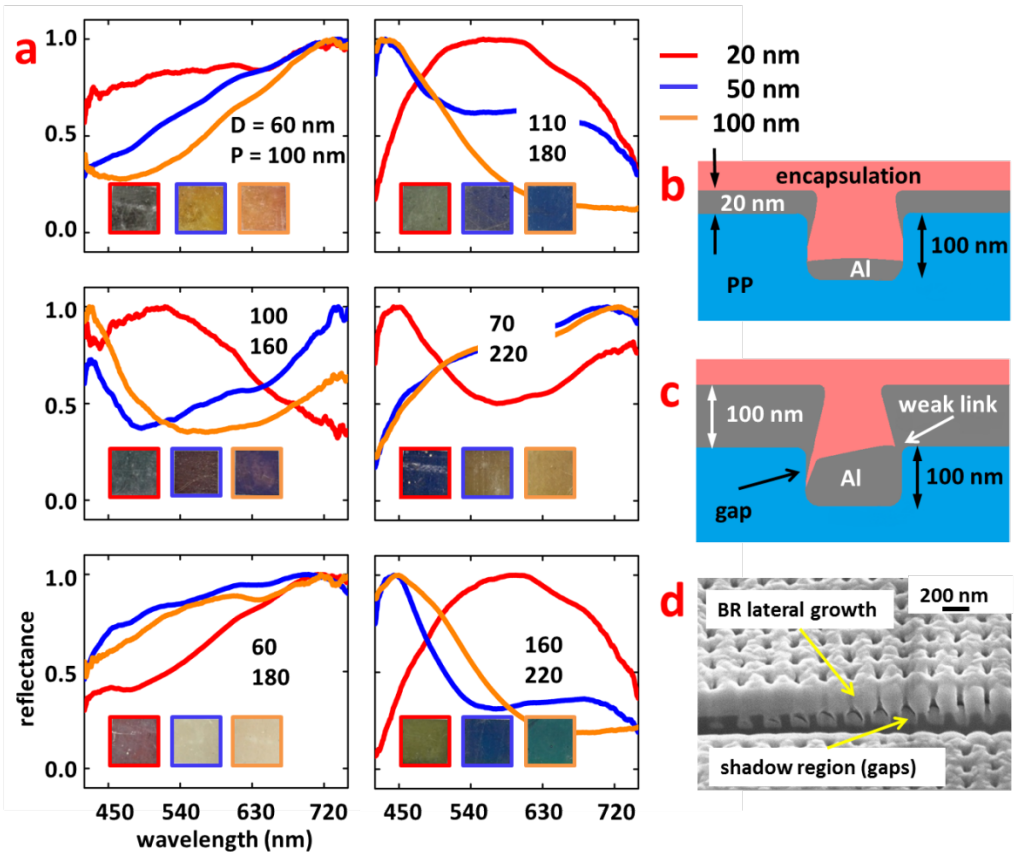

Figure 4. a: Measured reflectance spectra for batch metalized samples with different Al layer thickness, 20 nm, 50 nm, and 100 nm for six different combinations of lateral dimensions D and P. **b:** Schematic of realistic metal layer configuration for 20 nm Al in a directional evaporation process resulting in no connections between metal in the bottoms of the pits and the BR. **c:** Schematic of realistic metal layer configuration for 100 nm Al in a directional evaporation process resulting in weak link connections and gaps between metal in the pits and the BR. **d:** FIB-SEM image of a sample with ~200 nm Al thickness showing the presence of gaps and weak links and the shadowing effect.

For 100 nm Al samples both batch and R2R metallization yielded the same colors for the respective structures (**Figure S8)**. Whereas for R2R metallized 20 nm Al samples, all the structures yielded black or almost black colors and were not at all similar to the colors obtained from 20 nm batch metallized samples (**Figure S8)**. R2R thermal evaporation is less directional compared to

batch metallization, due to the curved nature of the foil roll substrate in comparison to the path of the evaporating vapor (**Figure S9**). In the R2R set-up used, the deposition angle varies, approximately, between +20° to -20° around the surface normal. This, however, did not change the metallization configuration for R2R 100 nm samples as compared to 100 nm batch metallized samples, due to the shadowing effect of the BR that was discussed earlier, hence still giving rise to links and variable gap configurations between the BR and Al pillars. The resulting colors from the 100 nm R2R samples are due to the same phenomenon of coupling between pillar and cavity resonances and hence give rise to the same colors as that of batch metallized samples of similar dimensions. For 20 nm R2R metallized samples, on the other hand, one can expect more sidewall coverage and relatively less metal at the bottom of the pits as opposed to the 20 nm batch metallized samples. This and due to the fact that the R2R metallized film is more grainy due to the high deposition rate, results in increased absorption in 20 nm films[39] and hence they appear dark. The above mentioned observations indicate that the weak link and varying gap configuration, in 100 nm Al samples, is most robust towards industrial R2R metallization. Once the process parameters have been optimized, the plasmonic color meta-surfaces could be fabricated with high (almost 100 %) yield. Hundreds of meters of foil were produced with identical color patches. Failure modes, when un-optimized process parameters are used during extrusion coating, comprise of: 1) mechanical abrasion of the structures on the shim, and 2) poor replication of structures in the polymer foil. In a commercial production scenario, such failure modes can easily be avoided by processing at optimum parameters.

Conclusion

We have demonstrated a high resolution plasmonic color metasurface design which is robust and has high tolerance towards high speed R2R fabrication, using Al nanostructures with dimensions below the optical diffraction limit. Various colors in the visible spectrum were obtained due to a coupling of pillar and cavity plasmon resonances. Nano structured polymer foils comprising pits with varying diameter and pitch were manufactured by a high throughput R2R-EC process. Subsequently, the structured foils were metallized with Al by a high-throughput R2R thermal evaporation process. Further, the foils were protected on the metallized side by a R2R thermal lacquering process. The demonstrated nano-architecture and technology can pave the way for plasmonic colors to be implemented in various applications and consumer products, and we

believe the technology has the potential to revolutionize the printing, display and flexible electronics industry.

Experimental

Master origination and extrusion coating

Pits of 100 nm depth, with varying D from 60 nm to 160 nm and P from 80 nm to 220 nm were fabricated on the surface of a polished 100 mm Si master wafer by e-beam lithography, using a positive e-beam resist (ZEP-520A), followed by deep reactive ion etching (DRIE). In order to achieve high writing speeds, potentially up to 1 cm^2/hour, a single spot exposure method was used during e-beam writing.[40, 41] The silicon masters were converted into low thermal conductivity resin R2R shims (Inmold A/S, Denmark) with opposite relief polarity to the Si master. The structures were then replicated in PP (WF420HMS, Borealis) on a transparent polyethylene terephthalate (PET) carrier foil, by R2R-EC on an extruder at Danapak A/S (Denmark) as described by Murthy et.al.[26] The extruder setup consists of a 25 mm extruder (BfA Plastic GmbH), 35 mm extruder (AXON Plastics Machinery AB), and an EPOCH nozzle with a respective 3-layer feedblock (Cloeren Inc.), During R2R-EC (shown in **Figure S1**), the polymer melt curtain is extruded through a flat die, then laminated onto a carrier foil by squeezing the melt between a nano-structured cooling roller kept below the solidification temperature of the polymer and a flexible counter roller. Finally, the structured foil is wound up on a winding roller. The structured foil presented, in this work was fabricated at the rate of 10 m/min, with the cooling roller temperature kept at 70 ^oC, counter roller force of 7 kN/m and polymer feed rate of 90 g/m2 @ 10 m/min, resulting in a PP film thickness of 150 μm.

Batch metallization

Individual foil samples with nano-pits (equivalent to the size of a 4” wafer), were cut out from the extruded PP foil rolls. Different thickness of Al layer, between 20 nm and 200 nm, was later evaporated on the structured polymer film by an e-beam evaporator (SCM600 Alcatel) at a rate of 10 Å/s (0.1 ng/s), monitored by quartz crystal microbalance during deposition. The chamber pressure during evaporation was ~10^{-8} bars.

R2R metallization

Similar nano-structured foils were also metallized with different Al thickness, between 20 nm and 100 nm, by R2R thermal evaporation (MET-LUX SA, Luxembourg). The process pressure was around 10^{-7} bars and deposition rate of ~1 g/s. The web speed was varied between 350 m/min and 500 m/min depending on the required metal thickness. For 100 nm Al samples, to avoid delamination of the metal layer, the foils were coated twice with 50 nm Al.

Encapsulation

To avoid mechanical scratching of the metal layer and to improve its stability for ambient use, samples were encapsulated. The cut out batch metallized samples were encapsulated using a thin layer (~few microns) of UV curable glue (NOA 61, Norland products). The R2R metallized foils were encapsulated using a commercial lacquer (Reflex 1350125-1, NC-LAK, Resino Trykfarver A/S, Denmark), by a R2R lacquering process (Danapak Flexibles A/S, Denmark).

Optical measurements

The sandwich structure was viewed from the backside through the carrier foil. When the structures are illuminated through the transparent carrier foil, different colors are perceived depending on the dimensions of the nano-pits in the foil and the thickness of the deposited Al layer. Reflectance spectra were obtained with a custom build spectrophotometer, featuring a broad band LED light source (MWWHL3, Thorlabs Inc., USA), a 50/50 beam splitter (CM1-BS013, Thorlabs Inc., USA) and a calibrated spectrometer (USB2000+VIS-NIR-ES, Ocean Optics Inc., USA). The LED provides unpolarized light in the range 420 nm to 750 nm, the beam splitter reflects the light to provide normal incidence on the sample, while the light reflected from the sample is transmitted through the beam splitter to the spectrometer. The spot size was around 1.5 mm in diameter. The reflectance of each sample was determined from the measured reflection intensity I_{meas}, corrected with a reference measurement based on the absolute reflection of a flat silicon wafer, I_{ref}, and a dark measurement without any sample, I_{dark}:

$$R_{total} = \frac{I_{meas} - I_{dark}}{I_{ref} - I_{dark}}. \qquad (1)$$

The reflectance measurements shown in this work are scaled to the maximum reflectance value for the corresponding samples. The spectra are smoothed with a moving average filter to reduce high frequency noise.

Simulations

Simulations were performed using a finite difference frequency domain solver from computer simulation technology (CST AG) microwave studio commercial software. The 3D model of the structures shown in **Figure 1g** was simulated. A linearly polarized plane wave at normal incidence was used as the light source, with intensity spectral data of the actual LED light source used for the measurements (**Figure S10**). A perfectly matched boundary condition was used in the plane of incidence, while a periodic boundary condition was used in the plane of the carrier foil. The material data for Al was obtained from Palik material hand book.[42] 40 The built-in dispersion model was used to fit the data in the specified frequency range (400 – 800 THz). The refractive indices of the polymer layers were assumed to be 1.55 for all layers. We see that the simulated spectra are in good agreement with the experimental ones.

FIB-SEM imaging

The FIB-SEM images shown in **Figure 2g** and **Figure 3d**, were made by a standard FIB-SEM imaging procedure, except that there was no platinum (Pt) protection layer used on top of the structures. A very low current was used during milling, in order not to damage or change the configuration of the structures as much as possible. This was deliberately done, to avoid any confusion between the deposited Al with Pt. The images were made using a Ziess Crossbeam 1540 EsB. In FIB-SEM the angle between the electron beam and the ion beam is 54°. The FIB crossection by Ga ions was made at 90° to the sample surface by tilting the sample stage to 54°. The cross-section was then viewed by SEM at 36° tilt, for the 54° stage tilt.

Electronic Supplementary Information

Extrusion coating – principle of operation, Comparison between constant versus varying gap configuration, Comparison of simulation spectra with sharp and rounded edges , Coupling between pillar and cavity plasmons, Diameter and depth variation at constant pitch and metal

thickness, Measured and simulated spectra for 20 nm samples, Comparison of R2R and batch metalized samples, R2R metallization – principle of operation, LED lamp spectrum.

Author contributions

SM fabricated the samples. SM made the computer simulations and recorded the SEM and FIB-SEM images. NF, JSM and PEH made the optical characterizations of the samples. HP, HCP and RT supervised SM. HP and RT conceived the project. SM and RT wrote the paper.

Acknowledgements

This work is supported by the Danish National Advanced Technology Foundation (HTF) through the "Advanced Technology Project LANI" (grant 011-2011-3), the "Advanced Technology Platform NanoPlast" (grant 007-2010-2), and by The Danish Ministry of Higher Education and Science, through an industrial PhD scholarship for Swathi Murthy (grant 1355-00143). Mr. Jesper Scheel is acknowledged for taking the photos presented in the paper. Dr. Nis K- Andersen is acknowledged for making the 3d sketch in **Figure 1e**.

Conflicts of interest

There are no conflicts to declare.

TOC graphic

Novel plasmonic metasurface design that allows roll-to-roll mass-production of plasmonic color foils at a line speed of 10 meters/minute.

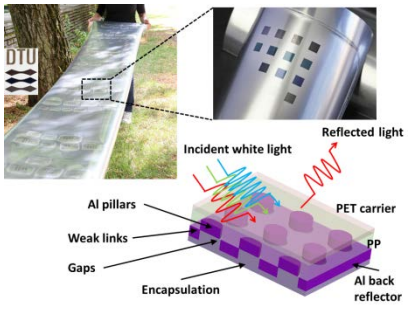

References

1. W. L. Barnes, *Journal of Optics a-Pure and Applied Optics*, 2006, **8**, S87-S93.
2. A. Kristensen, J. K. W. Yang, S. I. Bozhevolnyi, S. Link, P. Nordlander, N. J. Halas and N. A. Mortensen, *Nature Reviews Materials*, 2016, **2**, 16088.
3. O. Nicoletti, F. de la Pena, R. K. Leary, D. J. Holland, C. Ducati and P. A. Midgley, *Nature*, 2013, **502**, 80-+.
4. B. Luk'yanchuk, N. I. Zheludev, S. A. Maier, N. J. Halas, P. Nordlander, H. Giessen and C. T. Chong, *Nature Materials*, 2010, **9**, 707-715.
5. S. J. Tan, L. Zhang, D. Zhu, X. M. Goh, Y. M. Wang, K. Kumar, C. W. Qiu and J. K. W. Yang, *Nano Letters*, 2014, **14**, 4023-4029.
6. X. L. Zhu, C. Vannahme, E. Hojlund-Nielsen, N. A. Mortensen and A. Kristensen, *Nature Nanotechnology*, 2016, **11**, 325-+.
7. H. L. Hu, H. G. Duan, J. K. W. Yang and Z. X. Shen, *Acs Nano*, 2012, **6**, 10147-10155.
8. I. Zoric, M. Zach, B. Kasemo and C. Langhammer, *Acs Nano*, 2011, **5**, 2535-2546.
9. W. Caseri, *Macromolecular Rapid Communications*, 2000, **21**, 705-722.
10. M. A. Garcia, *Journal of Physics D-Applied Physics*, 2011, **44**.
11. K. Kumar, H. G. Duan, R. S. Hegde, S. C. W. Koh, J. N. Wei and J. K. W. Yang, *Nature Nanotechnology*, 2012, **7**, 557-561.
12. J. S. Clausen, E. Hojlund-Nielsen, A. B. Christiansen, S. Yazdi, M. Grajower, H. Taha, U. Levy, A. Kristensen and N. A. Mortensen, *Nano Letters*, 2014, **14**, 4499-4504.
13. R. J. H. Ng, S. J. Tan, X. M. Goh, J. K. W. Yang and Ieee, *9th International Congress on Advanced Electromagnetic Materials in Microwaves and Optics (Metamaterials 2015)*, 2015, 328-330.
14. F. S. Ou, M. Hu, I. Naumov, A. Kim, W. Wu, A. M. Bratkovsky, X. M. Li, R. S. Williams and Z. Y. Li, *Nano Letters*, 2011, **11**, 2538-2542.
15. H. Ko, S. Singamaneni and V. V. Tsukruk, *Small*, 2008, **4**, 1576-1599.
16. E. Hutter and J. H. Fendler, *Advanced Materials*, 2004, **16**, 1685-1706.
17. K. M. Mayer and J. H. Hafner, *Chemical Reviews*, 2011, **111**, 3828-3857.
18. W. L. Barnes, A. Dereux and T. W. Ebbesen, *Nature*, 2003, **424**, 824-830.
19. J. Sauvage-Vincent, Y. Jourlin, S. Tonchev, C. Veillas, C. Pedri and O. Parriaux, Brussels, BELGIUM, 2012.
20. J. Sauvage-Vincent, S. Tonchev, C. Veillas, S. Reynaud and Y. Jourlin, *Journal of the European Optical Society-Rapid Publications*, 2013, **8**.
21. M. W. Knight, L. F. Liu, Y. M. Wang, L. Brown, S. Mukherjee, N. S. King, H. O. Everitt, P. Nordlander and N. J. Halas, *Nano Letters*, 2012, **12**, 6000-6004.
22. J. Olson, A. Manjavacas, L. F. Liu, W. S. Chang, B. Foerster, N. S. King, M. W. Knight, P. Nordlander, N. J. Halas and S. Link, *Proceedings of the National Academy of Sciences of the United States of America*, 2014, **111**, 14348-14353.
23. D. Franklin, Y. Chen, A. Vazquez-Guardado, S. Modak, J. Boroumand, D. M. Xu, S. T. Wu and D. Chanda, *Nature Communications*, 2015, **6**.
24. J. F. Zhang, J. Y. Ou, N. Papasimakis, Y. F. Chen, K. F. MacDonald and N. I. Zheludev, *Optics Express*, 2011, **19**, 23279-23285.
25. X. M. Goh, R. J. H. Ng, S. H. Wang, S. J. Tan and J. K. W. Yang, *Acs Photonics*, 2016, **3**, 1000-1009.
26. S. Murthy, M. Matschuk, Q. Huang, N. K. Mandsberg, N. A. Feidenhans'l, P. Johansen, L. Christensen, H. Pranov, G. Kofod, H. C. Pedersen, O. Hassager and R. Taboryski, *Advanced Engineering Materials*, 2016, **18**, 484-489.
27. A. Telecka, S. Murthy, L. Schneider, H. Pranov and R. Taboryski, *Acs Macro Letters*, 2016, **5**, 1034-1038.
28. S. Murthy, H. Pranov, H. C. Pedersen and R. Taboryski, *Journal of Vacuum Science & Technology B*, 2016, **34**.

29. E. C. Højlund-Nielsen, Jeppe, T. Mäkela, L. H. Thamdrup, M. Zalkovskij, T. Nielsen, N. Li Pira, J. Ahopelto, N. A. Mortensen and A. Kristensen, *Advanced Materials Technologies*, 2016.
30. S. H. Ahn and L. J. Guo, *Advanced Materials*, 2008, **20**, 2044-+.
31. M. Leitgeb, D. Nees, S. Ruttloff, U. Palfinger, J. Götz, R. Liska, M. R. Belegratis and B. Stadlober, *ACS Nano*, 2016, **DOI: 10.1021/acsnano.5b07411**.
32. R. Esteban, A. G. Borisov, P. Nordlander and J. Aizpurua, *Nature Communications*, 2012, **3**.
33. H. G. Duan, H. L. Hu, K. Kumar, Z. X. Shen and J. K. W. Yang, *Acs Nano*, 2011, **5**, 7593-7600.
34. A. L. Koh, A. I. Fernandez-Dominguez, D. W. McComb, S. A. Maier and J. K. W. Yang, *Nano Letters*, 2011, **11**, 1323-1330.
35. J. A. Schuller, E. S. Barnard, W. S. Cai, Y. C. Jun, J. S. White and M. L. Brongersma, *Nature Materials*, 2010, **9**, 193-204.
36. E. Prodan, C. Radloff, N. J. Halas and P. Nordlander, *Science*, 2003, **302**, 419-422.
37. R. M. Hill, *Nature*, 1966, **210**, 512-&.
38. G. M. Whitesides and B. Grzybowski, *Science*, 2002, **295**, 2418-2421.
39. K. L. Kelly, E. Coronado, L. L. Zhao and G. C. Schatz, *Journal of Physical Chemistry B*, 2003, **107**, 668-677.
40. N. Gadegaard, S. Thoms, D. S. Macintyre, K. McGhee, J. Gallagher, B. Casey and C. D. W. Wilkinson, *Microelectronic Engineering*, 2003, **67-8**, 162-168.
41. E. Hojlund-Nielsen, T. Greibe, N. A. Mortensen and A. Kristensen, *Microelectronic Engineering*, 2014, **121**, 104-107.
42. D. Y. Smith, E. Shiles and M. Inokuti, in *Handbook of Optical Constants of Solids*, Academic Press, Burlington, 1997, pp. 369-406.